Pergamon

Int. J. Heat Mass Transfer. Vol. 40, No. 12, pp. 2887–2900, 1997

Printed in Great Britain
0017 9310/97 $17.00 + 0.00

PII: S0017-9310(96)00325-0

Numerical and analytical investigation of vapor flow in a disk-shaped heat pipe incorporating secondary flow

N. ZHU and K. VAFAI†

Department of Mechanical Engineering, The Ohio State University, Columbus, OH 43210, U.S.A.

(*Received* 25 *June* 1996 *and in final form* 10 *September* 1996)

Abstract—This paper presents a three-dimensional numerical analysis and a pseudo-three-dimensional analytical modeling of the steady incompressible vapor flow in an asymmetrical disk-shaped heat pipe heated from the top center area. The nonlinear differential elliptical equations of motion and the continuity equation were solved numerically over the entire vapor flow domain. Discretization of the governing equations was achieved using a finite element scheme based on the Galerkin method of weighted residuals. The analytical model involves the use of the boundary layer approximation and the bifurcation of the flow field on the r–y plane to describe the velocity profile under conditions including strong flow reversal. For both numerical and analytical studies, backflow was observed at the top entrance of the condensation zone for injection Reynolds number of 50 and higher. The three-dimensional effects and the effects of the secondary flow formation are discussed in this work. The numerical and analytical results establish that the pressure variations in the angular and transverse directions for a typical disk-shaped heat pipe are small and can be neglected. A very good agreement was found between the numerical results and the analytical results. The analytical model saves tremendous computer time compared with the numerical simulation, which requires CPU times five orders of magnitude larger than those for the analytical model. © 1997 Elsevier Science Ltd.

INTRODUCTION

The study of vapor flow characteristics is important in establishing the heat transfer limits for heat pipes. There have been numerous investigations connected with the problem of vapor flow in conventional symmetrical heat pipes. Different approach techniques such as similarity analysis, perturbation techniques, series expansions, transformation techniques, and numerical methods have been used in the vapor flow analysis.

Only a few investigators have studied the vapor flow in asymmetrical heat pipes, which is a more complicated and less understood system. The only numerical study pertinent to the vapor flow in an asymmetrical heat pipe found in open literature is reported by Ooijen and Hoogendoorn [1]. In their work, a two-dimensional investigation was carried out for steady incompressible laminar vapor flow in a flat plate heat pipe with an adiabatic top plate. The mass and momentum equations were solved with the control volume finite difference approach. Results were reported for the injection (radial) Reynolds number over the range of $1 \leqslant Re_r \leqslant 50$. Their results show that the velocity profiles are nonsimilar and asymmetrical for injection (radial) Reynolds number $Re_r > 1$. Flow reversal is encountered in the condenser section at $Re_r > 10$.

Due to the viscous shearing effects at the side walls, a three-dimensional analysis is preferred for the vapor flow in asymmetrical flat plate as well as disk-shaped heat pipes. To the best of the authors' knowledge, the three-dimensional numerical analysis of the vapor flow in heat pipes, regardless of its type, has not been reported so far. Vafai *et al.* [2–5] have carried out an analytical study for incompressible vapor and liquid flow in both flat plate and disk-shaped heat pipes, which are heated either from the top surface or from the bottom surface. They developed a pseudo-three-dimensional analytical model based on an in-depth integral analysis and the method of matched asymptotic expansions. The vapor flow field was bifurcated on the x–y (r–y) plane due to the asymmetrical feature of heat source and sinks. The parabolic velocity profiles, which vary with the distance along the heat pipe, were used for both upper and lower parts of vapor flow within the heat pipes. The hydrodynamic coupling of the vapor and liquid phase, the effects of nonDarcian transport through the porous wicks and the gravitational effects are incorporated in their model. Analytical results for the shifted vapor velocity profiles, the vapor and liquid pressure distributions along the heat pipes were obtained. Their results show

† Author to whom correspondence should be addressed.

NOMENCLATURE

A_1	coefficient defined by equation (22)
A_2	coefficient defined by equation (23)
A_3	coefficient defined by equation (24)
a_3	coefficient used in the velocity profile for $0 < y < f$ region
B_1	coefficient defined by equation (25)
B_2	coefficient defined by equation (26)
b_3	coefficient used in the velocity profile for $f < y < h$ region
D_2	constant defined by equation (27)
f	location of the maximum vapor velocity [m]
h	height of vapor channel [m]
p	pressure [Pa]
r, y	radial and vertical coordinates [m]
R	radius of the disk-shaped heat pipe [m]
R_e	radius of the evaporation zone [m]
Re_h	injection Reynolds number, $\rho v_1 h/\mu$
u, v, w	radial, vertical, angular velocity components [m s^{-1}]
U	the maximum radial velocity component [m s^{-1}]
u^+	dimensionless radial velocity component, u/u_1
u_1	characteristic value for radial velocity component, $v_1 R/h$
v_1	vapor injection velocity [m s^{-1}]
v_2	vapor suction velocity [m s^{-1}].

Greek symbols

φ	ratio of the radius of the evaporation zone to the heat pipe radius, R_e/R
Φ	angle of each divergent flow channel of the disk-shape heat pipe
μ	dynamic viscosity [N s m^{-2}]
θ	angular coordinate
ρ	density [kg m^{-3}].

Superscript

+	dimensionless quantity.

that the effects of vapor–liquid hydrodynamic coupling on the vapor flow is negligible [5].

It is well recognized that zero wall shear stress and flow reversal occur in heat pipe condenser section at low injection Reynolds number. Quaile and Levy [6] have investigated incompressible flow in cylindrical tubes with porous walls. They found that flow reversal appears for $Re_r > 2.5$ and the regions of reverse flow are unstable and undergo transition to turbulence. Numerical analysis of the vapor flow in conventional cylindrical heat pipes by Bankston and Smith [7] predicted flow reversal in the condenser section for $Re_r > 2$. Analysis by Ooijen and Hoogendoorn [1] also show flow reversal in an asymmetrical flat plate heat pipe for $Re_r > 10$. Busse and Loehrke [8] developed an analytical model for predicting laminar, subsonic vapor flow in axisymmetric cylindrical heat pipe condensers. Their model is based on the boundary layer approximation and the use of a non-continuous power series to describe the vapor velocity profile under conditions including strong flow reversal.

In the present study, the complete problem of the three-dimensional vapor flow in an asymmetrical disk-shaped heat pipe is analyzed numerically. The nonlinear differential elliptical equations of motion are solved over the entire vapor flow channel in order to allow all of the features of the incompressible laminar vapor flow to be taken into account. Also, the pseudo-three-dimensional analytical model developed by Vafai *et al.* [2–5] is extended to laminar flow predictions for strong flow reversal. The modified analytical model, while saving tremendous computer time (more than five orders reduction in CPU time), predicts the velocity variation and pressure drop accurately along the disk-shaped heat pipe.

NUMERICAL ANALYSIS

Governing equations

The physical problem under consideration is a horizontal disk-shaped heat pipe, as shown in Fig. 1. Heat input is over a circular area on the top center surface of the heat pipe, so that the vapor flow becomes asymmetrical. The vapor space is divided into several channels by the vertical wicks which transport liquid from the bottom wick to the top wick. Any one of the internal channels can be considered as a building block for the disk-shaped heat pipe. Once the fluid flow characteristics within one of the channels is determined, the fluid flow characteristics of the entire heat pipe can be easily established. The results of this analysis are applicable to any number of channels.

Steady, incompressible, three-dimensional laminar vapor flow in a channel is considered, as shown in Fig. 1(b). The transport properties of the fluid are assumed to be constant. The vapor injection and suction rates are assumed uniform on the top and bottom surfaces of the vapor channel and negligible on the vertical surfaces. The differential equations associated with this three-dimensional problem are the continuity and the momentum equations. In cylindrical coordinates the governing equations are

$$\frac{\partial u}{\partial r} + \frac{\partial v}{\partial y} + \frac{1}{r}\frac{\partial w}{\partial \theta} + \frac{u}{r} = 0 \qquad (1)$$

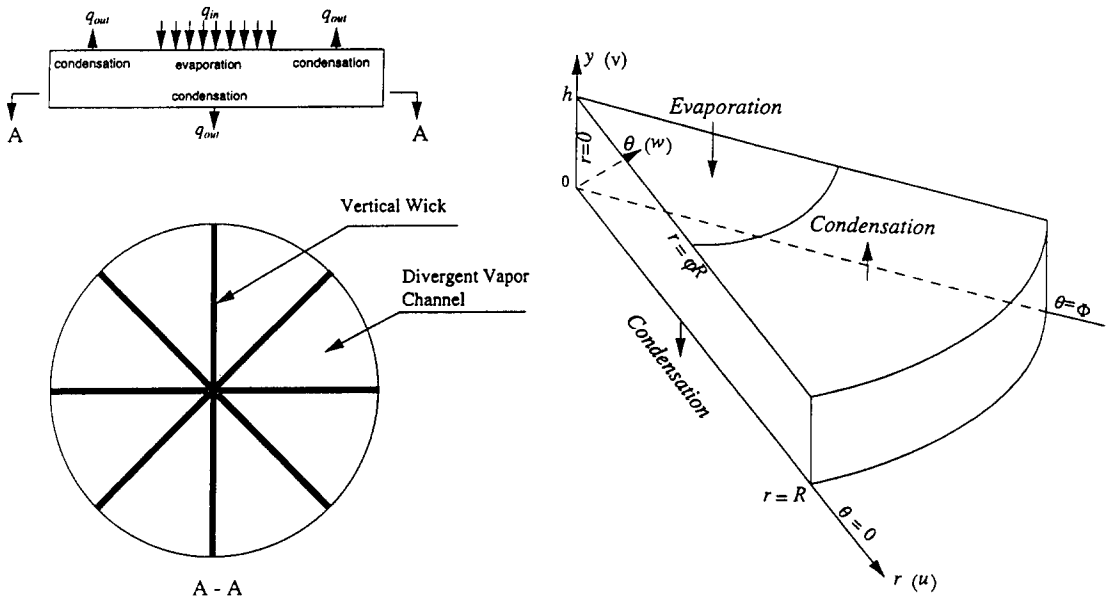

Fig. 1. Schematic of the disk-shaped heat pipe: (a) configuration of the heat pipe; (b) the coordinate system used in the analysis.

$$\rho\left(u\frac{\partial u}{\partial r}+v\frac{\partial u}{\partial y}+\frac{w}{r}\frac{\partial u}{\partial \theta}-\frac{w^2}{r}\right)=-\frac{\partial p}{\partial r}$$
$$+\mu\left(\frac{\partial^2 u}{\partial r^2}+\frac{1}{r}\frac{\partial u}{\partial r}+\frac{\partial^2 u}{\partial y^2}+\frac{1}{r^2}\frac{\partial^2 u}{\partial \theta^2}-\frac{u}{r^2}-\frac{2}{r^2}\frac{\partial w}{\partial \theta}\right) \quad (2)$$

$$\rho\left(u\frac{\partial v}{\partial r}+v\frac{\partial v}{\partial y}+\frac{w}{r}\frac{\partial v}{\partial \theta}\right)=-\frac{\partial p}{\partial y}$$
$$+\mu\left(\frac{\partial^2 v}{\partial r^2}+\frac{1}{r}\frac{\partial v}{\partial r}+\frac{\partial^2 v}{\partial y^2}+\frac{1}{r^2}\frac{\partial^2 v}{\partial \theta^2}\right) \quad (3)$$

$$\rho\left(u\frac{\partial w}{\partial r}+v\frac{\partial w}{\partial y}+\frac{w}{r}\frac{\partial w}{\partial \theta}+\frac{uw}{r}\right)=-\frac{1}{r}\frac{\partial p}{\partial \theta}$$
$$+\mu\left(\frac{\partial^2 w}{\partial r^2}+\frac{1}{r}\frac{\partial w}{\partial r}+\frac{\partial^2 w}{\partial y^2}+\frac{1}{r^2}\frac{\partial^2 w}{\partial \theta^2}\right.$$
$$\left.+\frac{2}{r^2}\frac{\partial u}{\partial \theta}-\frac{w}{r^2}\right). \quad (4)$$

Boundary conditions

The boundary conditions are:

$$u(0,y,\theta)=v(0,y,\theta)=w(0,y,\theta)=0$$
$$u(R,y,\theta)=v(R,y,\theta)=w(R,y,\theta)=0$$
$$u(r,y,0)=v(r,y,0)=w(r,y,0)=0$$
$$u(r,y,\Phi)=v(r,y,\Phi)=w(r,y,\Phi)=0$$
$$u(r,0,\theta)=w(r,0,\theta)=0$$
$$v(r,0,\theta)=-v_2$$
$$u(r,h,\theta)=w(r,h,\theta)=0$$

$$v(r,h,\theta)=\begin{cases}-v_1, & 0\leqslant r\leqslant \varphi R\\ v_2, & \varphi R\leqslant r\leqslant R\end{cases}$$

$$p(0,h/2,\theta)=0. \quad (5)$$

The analysis by Zhu and Vafai [5] revealed that the effect of vapor–liquid hydrodynamic coupling on the vapor flow is negligible. Therefore the nonslip boundary conditions are used at the vapor–liquid interfaces. The vapor injection velocity v_1 is related to the input power Q_{in} by the following relation:

$$v_1=\frac{Q_{in}}{\rho h_{fg}\pi R_e^2}. \quad (6)$$

The vapor suction velocity v_2 is obtained by the mass balance which requires the fluid that is entering in the evaporator section to flow out through the condenser section.

Numerical scheme

The discretization of the set of governing equations (1)–(4) along with the boundary conditions was carried out by using a finite element formulation based on the Galerkin method of weighted residuals. The finite element mesh used in the present study is shown in Fig. 2. The 27-node quadratic elements were used for discretizing the computational domain, resulting in a triquadratic interpolation for the velocity. A trilinear interpolation was used for the pressure approximations. A variable mesh grading strategy was adopted to capture the sharper gradients in the velocity and pressure at both ends of the evaporator section and the entrance region of the condenser section. To confirm the grid independence of the three-

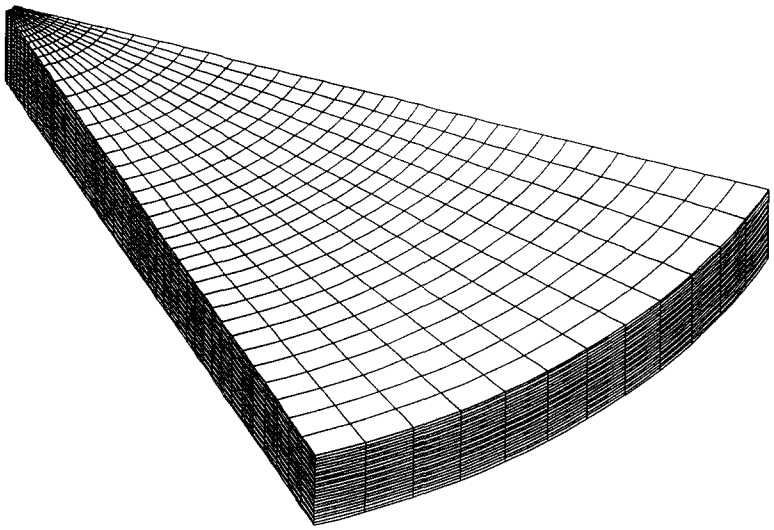

Fig. 2. Finite element mesh used with the numerical computations.

dimensional model, results were obtained by increasing the grid points from the $81\times25\times25$ mesh to a $161\times49\times49$ mesh. A comparison of magnitudes of the vapor velocity and pressure for various runs showed that these values change by less than 1%, thus indicating that the grid structure is sufficiently fine.

The discretization of the governing equations along with the boundary conditions results in a highly nonlinear, coupled system of algebraic equations. This system of equations was then solved by using an iterative solution scheme based on the segregated solution algorithm. Basically, this scheme involves decomposition of the entire system of equations into smaller subsystems. Each subsystem is then solved by using an iterative solver. Convergence was assumed to have been reached when the relative change in variables between consecutive iterations was 10^{-3}. The application of the Galerkin-based FEM is well described by Taylor and Hood [9], and its application in the finite-element code used in the present work is also well documented [10].

ANALYTICAL SOLUTION

Mathematical formulation and modeling

Based on physical considerations, the vapor injection/suction on the vertical wicks is negligible. Therefore, the θ component of the vapor velocity is negligible and the system of equations of motion in the dimensionless variables

$$r^+=\frac{r}{R},\quad y^+=\frac{y}{h},\quad \theta^+=\frac{\theta}{\Phi},$$

$$u^+=\frac{u}{u_1},\quad v^+=\frac{v}{v_1},\quad p^+=\frac{p}{\rho u_1^2} \tag{7}$$

reduces to the form

$$\frac{\partial u^+}{\partial r^+}+\frac{\partial v^+}{\partial y^+}+\frac{u^+}{r^+}=0 \tag{8}$$

$$u^+\frac{\partial u^+}{\partial r^+}+v^+\frac{\partial u^+}{\partial y^+}=-\frac{\partial p^+}{\partial r^+}+\frac{1}{Re_h}\frac{\partial^2 u^+}{\partial (y^+)^2}+\frac{Re_h}{Re_1^2}\times\left(\frac{\partial^2 u^+}{\partial (r^+)^2}+\frac{1}{r^+}\frac{\partial u^+}{\partial r^+}+\frac{1}{(r^+)^2}\frac{\partial^2 u^+}{\partial(\theta^+)^2}-\frac{u^+}{(r^+)^2}\right) \tag{9}$$

$$\frac{Re_h^2}{Re_1^2}\left(u^+\frac{\partial v^+}{\partial r^+}+v^+\frac{\partial v^+}{\partial y^+}\right)=-\frac{\partial p^+}{\partial y^+}+\frac{Re_h}{Re_1^2}\frac{\partial^2 v^+}{\partial (y^+)^2}+\frac{Re_h^3}{Re_1^4}\left(\frac{\partial^2 v^+}{\partial (r^+)^2}+\frac{1}{r^+}\frac{\partial v^+}{\partial r^+}+\frac{1}{(r^+)^2}\frac{\partial^2 v^+}{\partial(\theta^+)^2}\right) \tag{10}$$

$$0=-\frac{\partial p^+}{\partial \theta^+}+\frac{Re_h}{Re_1^2}\frac{2}{r^+}\frac{\partial u^+}{\partial \theta^+} \tag{11}$$

where

$$u_1=\frac{R}{h}v_1,\quad Re_h=\frac{\rho v_1 h}{\mu},\quad Re_1=\frac{\rho u_1 h}{\mu}.$$

To obtain an analytical solution for the asymmetrical disk-shaped heat pipe, we note that the heat pipe is long enough such that the vapor injection Reynolds number Re_h is small with respect to Re_1. In this case, which covers most practical situations, equations (9)–(11) reduce to the form

$$u^+\frac{\partial u^+}{\partial r^+}+v^+\frac{\partial u^+}{\partial y^+}=-\frac{\partial p^+}{\partial r^+}+\frac{1}{Re_h}\frac{\partial^2 u^+}{\partial (y^+)^2} \tag{12}$$

$$\frac{\partial p^+}{\partial y^+}=0 \tag{13}$$

$$\frac{\partial p^+}{\partial \theta^+}=0. \tag{14}$$

This indicates that the vapor flow in a long heat pipe can be calculated on the basis of the simpler system of equations for a boundary layer. The validity of the boundary layer approximation was examined by Busse and Prenger [11]. Good agreement was obtained between the pressure distribution along the axis of a cylindrical condenser predicted by using the boundary layer equations and those obtained using the Navier–Stokes equations for the ratio of the condenser length to its diameter as small as 2.5. The two-dimensional numerical study by Ooijen and Hoogendoorn [1] also revealed negligible transverse pressure difference in the y direction for the vapor flow in an asymmetrical flat plate heat pipe.

The boundary conditions (5) in the dimensionless form reduce to:

$$\begin{aligned}
&u^+(0,y^+,\theta^+) = u^+(1,y^+,\theta^+) = 0\\
&u^+(r^+,0,\theta^+) = u^+(r^+,1,\theta^+) = 0\\
&u^+(r^+,y^+,0) = u^+(r^+,y^+,1) = 0\\
&v^+(r^+,0,\theta^+) = -v_2^+\\
&v^+(r^+,1,\theta^+) = \begin{cases} -1, & 0 \leqslant r^+ \leqslant \varphi \\ v_2^+, & \varphi \leqslant r^+ \leqslant 1 \end{cases}\\
&p^+(0,y^+,\theta^+) = 0.
\end{aligned} \tag{15}$$

It should be noted again that in the present work the full set of governing equations (1)–(4) were solved numerically along with boundary conditions given by equation (5). Equations (12)–(14) along with boundary conditions given in equation (15) is a set for obtaining the analytical solution.

Solution method

For the analytical solution, the velocity profile is approximated by a functional product in the r^+, y^+, θ^+ directions

$$\begin{aligned}
u^+(r^+,y^+,\theta^+) = U^+(r^+)&(a_0(r^+)\\
&+a_1(r^+)y^+ + a_2(r^+)(y^+)^2 + a_3(r^+)(y^+)^3)\\
&\times(c_0 + c_1\theta^+ + c_2(\theta^+)^2)
\end{aligned} \tag{16}$$

where $U^+(r^+)$ denotes the maximum radial velocity component on each transverse surface along the r^+ direction. A third-order polynomial is used in equation (16) to account for the flow reversal in the r^+–y^+ plane. Due to the vapor injection from the heating side of the top wick, the location of the maximum vapor velocity $U^+(r^+)$ will be shifted towards the bottom wick within the $0 \leqslant r^+ \leqslant \varphi$ region. As the vapor flows downstream, the location of $U^+(r^+)$ will gradually shift towards the center in the y^+ direction due to the presence of symmetrical cooling conditions. To account for this feature, the vapor velocity profile in the y^+ direction is divided into two parts based on the location of the maximum vapor velocity: the lower part $(0 \leqslant y^+ \leqslant f^+(r^+))$ and the upper part $(f^+(r^+) \leqslant y^+ \leqslant 1)$. The location of the maximum vapor velocity, $y^+ = f^+(r^+)$, is also the location corresponding to zero shear stress for the velocity distribution on the r^+–y^+ plane. Applying the nonslip boundary conditions and

$$u^+(r^+,f^+(r^+),\tfrac{1}{2}) = U^+(r^+), \quad \left.\frac{\partial u^+}{\partial y^+}\right|_{y^+=f^+(r^+)} = 0 \tag{17}$$

to equation (16) results in the following velocity profile

$$u^+(r^+,y^+,\theta^+) = \begin{cases}
4U^+(r^+)\left\{a_3(r^+)\dfrac{y^+}{f^+} + \left(1 - a_3(r^+)\dfrac{y^+}{f^+}\right)\right.\\
\quad\left.\times\left[2\dfrac{y^+}{f^+} - \left(\dfrac{y^+}{f^+}\right)^2\right]\right\}(\theta^+ - (\theta^+)^2)\\
\qquad\qquad (0 \leqslant y^+ \leqslant f^+)\\
4U^+(r^+)\left\{b_3(r^+)\dfrac{1-y^+}{1-f^+} + \left(1 - b_3(r^+)\dfrac{1-y^+}{1-f^+}\right)\right.\\
\quad\left.\times\left[2\dfrac{1-y^+}{1-f^+} - \left(\dfrac{1-y^+}{1-f^+}\right)^2\right]\right\}(\theta^+ - (\theta^+)^2)\\
\qquad\qquad (f^+(r^+) \leqslant y^+ \leqslant 1)
\end{cases} \tag{18}$$

The coefficients $a_3(r^+)$ and $b_3(r^+)$ are then obtained using the momentum equations (12) and (13). According to equation (13) $\partial p^+/\partial r^+$ must be independent of y^+. Since it is impossible to satisfy equation (13) exactly with the polynomial velocity profile (18), we only require exact satisfaction of the relations

$$\left.\frac{\partial p^+}{\partial r^+}\right|_{y^+=0} = \left.\frac{\partial p^+}{\partial r^+}\right|_{y^+=1} = \frac{\partial \bar{p}^+}{\partial r^+} \tag{19}$$

instead of equation (13), where the derivatives are determined with the help of equations (12), (14) and (18) and the bar denotes the average

$$\bar{p}^+ = \frac{1}{r^+}\int_0^1\int_0^1 p^+ r^+ \,\mathrm{d}y^+\,\mathrm{d}\theta^+.$$

After a transformation we obtain the following equations for $a_3(r^+)$ and $b_3(r^+)$:

$$\begin{aligned}
\frac{\mathrm{d}a_3}{\mathrm{d}r^+} = \frac{-1}{2A_1(r^+)a_3 + A_2(r^+)}&\left\{\frac{5}{4U^+(r^+)Re_h}\right.\\
&\times\left(\frac{a_3+2}{f^+(r^+)} + \frac{b_3+2}{1-f^+(r^+)}\right)\\
&+\frac{5}{4U^+(r^+)(f^+(r^+))^2}\left[\left(v_2^+ f^+(r^+) - \frac{4}{Re_h}\right)a_3\right.
\end{aligned}$$

$$+2\left(v_2^+ f^+(r^+)-\frac{1}{Re_h}\right)\Bigg]+\left(a_3^2\frac{dA_1}{dr^+}+a_3\frac{dA_2}{dr^+}+\frac{dA_3}{dr^+}\right)+(A_1(r^+)a_3^2+A_2(r^+)a_3+A_3(r^+))\left(\frac{2}{U^+(r^+)}\frac{dU^+}{dr^+}+\frac{1}{r^+}\right)\Bigg\} \quad (20)$$

and

$$b_3(r^+)=B_1(r^+)a_3(r^+)+B_2(r^+) \quad (21)$$

where

$$A_1(r^+)=[f^+(r^+)+B_1^2(r^+)(1-f^+(r^+))]/105 \quad (22)$$

$$A_2(r^+)=\{4B_1(r^+)B_2(r^+)(1-f^+(r^+))+21[f^+(r^+)+B_1(r^+)(1-f^+(r^+))]\}/210 \quad (23)$$

$$A_3(r^+)=[B_2(r^+)(2B_2(r^+)+21)\times(1-f^+(r^+))+112]/210 \quad (24)$$

$$B_1(r^+)=\frac{\left(v_2^+ f^+(r^+)-\frac{4}{Re_h}\right)\Big/(f^+(r^+))^2}{\left[D_2(1-f^+(r^+))-\frac{4}{Re_h}\right]\Big/(1-f^+(r^+))^2} \quad (25)$$

$$B_2(r^+)=\frac{2\left(v_2^+ f^+(r^+)-\frac{1}{Re_h}\right)\Big/(f^+(r^+))^2-2\left[D_2(1-f^+(r^+))-\frac{1}{Re_h}\right\}\Big/(1-f^+(r^+))^2}{\left[D_2(1-f^+(r^+))-\frac{4}{Re_h}\right]\Big/(1-f^+(r^+))^2} \quad (26)$$

$$D_2=\begin{cases}-1, & 0\leqslant r^+\leqslant\varphi\\ v_2^+, & \varphi\leqslant r^+\leqslant 1\end{cases}. \quad (27)$$

The maximum vapor velocity $U^+(r^+)$ is determined by integrating the continuity equation (8). Utilizing the velocity profile given by equation (18) and the boundary conditions (15), the integration of the continuity equation (8) with respect to y^+ from 0 to 1 and θ^+ from 0 to 1 yields:

$$U^+(r^+)=\begin{cases}\dfrac{9(1-v_2^+)}{[a_3(r^+)f^+(r^+)+b_3(r^+)(1-f^+(r^+))+8]}r^+, & 0\leqslant r^+\leqslant\varphi\\ \dfrac{18v_2^+}{[a_3(r^+)f^+(r^+)+b_3(r^+)(1-f^+(r^+))+8]}\dfrac{1-(r^+)^2}{r^+}, & \varphi\leqslant r^+\leqslant 1\end{cases} \quad (28)$$

The location of the maximum vapor velocity, $f^+(r^+)$, is determined by integrating the r^+-momentum equation (12) with respect to y^+ from 0 to $f^+(r^+)$ and with respect to θ^+ from 0 to 1. The integration of the momentum equation (12) using the velocity profile (18) and boundary conditions (15) results in the following expression for the rate of change of $f^+(r^+)$

$$\frac{df^+(r^+)}{dr^+}=\frac{-1}{4a_3^2(r^+)+7a_3(r^+)-56}\times\Bigg\{\Bigg[(8a_3(r^+)+7)\frac{da_3(r^+)}{dr^+}+\frac{(8a_3^2(r^+)+49a_3(r^+)+168)}{U^+(r^+)}\frac{dU^+(r^+)}{dr^+}+\frac{1}{r^+}(4a_3^2(r^+)+7a_3(r^+)-56)+\frac{1575}{2(U^+(r^+))^2}\frac{dp^+}{dr^+}\Bigg]f^+(r^+)+\frac{525}{U^+(r^+)}\left(\frac{a_3(r^+)+2}{Re_h}\frac{1}{f^+(r^+)}-v_2^+\right)\Bigg\}. \quad (29)$$

The vapor pressure distribution is obtained by integrating the r^+-momentum equation (12) over the entire transverse section. Utilizing the derived velocity profile given in equation (18) and the boundary conditions given in equation (15), the integration of the momentum equation (12) with respect to y^+ from 0 to 1 and with respect to θ^+ from 0 to 1 yields

$$\frac{dp^+}{dr^+}=\frac{-4}{1575r^+}\frac{d}{dr^+}\{r^+(U^+(r^+))^2[(2a_3^2(r^+)+21a_3(r^+)+112)f^+(r^+)+(2b_3^2(r^+)+21b_3(r^+)+112)(1-f^+(r^+))]\}-\frac{2U^+(r^+)}{3Re_h}\left(\frac{a_3(r^+)+2}{f^+(r^+)}+\frac{b_3(r^+)+2}{1-f^+(r^+)}\right). \quad (30)$$

The set of differential equations (20), (29) and (30), is integrated simultaneously by using a fourth-order Runge–Kutta scheme.

RESULTS AND DISCUSSION

The results in Figs. 3–9 are based on a disk-shaped heat pipe with heavy water as the working fluid. The respective dimensions of the heat pipe are chosen as: $R=0.25$ m, $R_e=0.125$ m, $h=0.025$ m and $\Phi=45°$. The results in Figs. 3–9 were obtained for the operating temperature of 80°C and for Re_h values of 10, 25, 50, 75, 100 and 150.

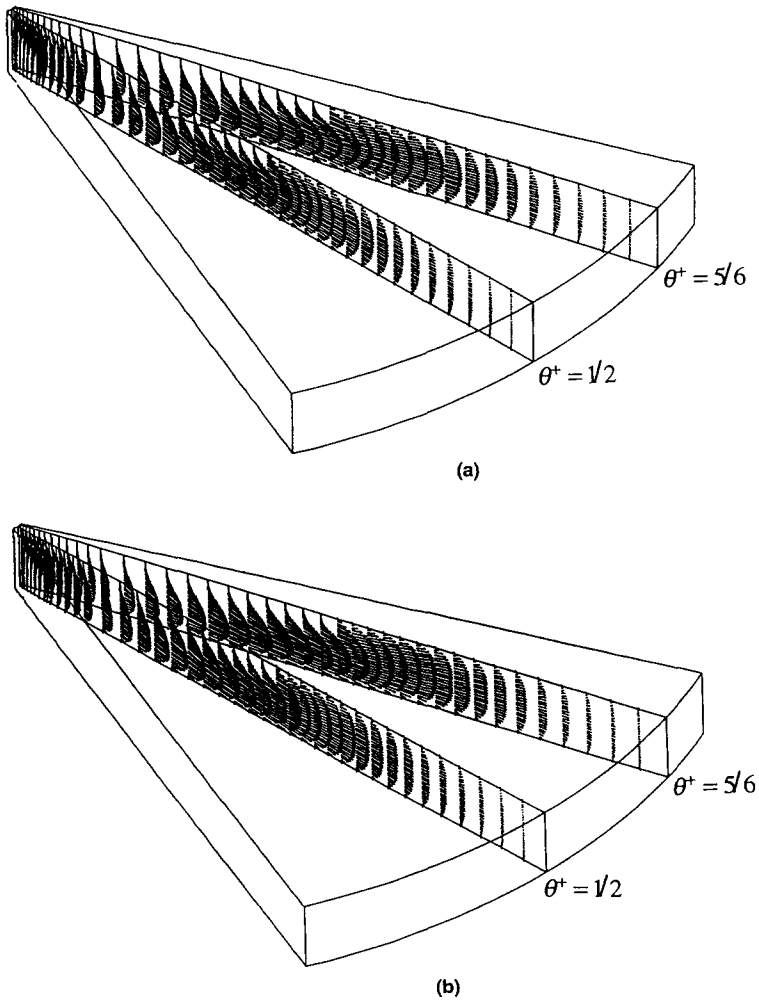

Fig. 3. Vapor flow field in the disk-shaped heat pipe for: (a) $Re_h = 10$; and (b) $Re_h = 25$.

Numerical results

The three-dimensional structure of the vapor flow field is presented in Figs. 3 and 4 by showing the velocity vector field in r–y planes. It should be noted that the magnitudes of the velocity profiles cannot be directly compared because the perspectives are not normal to the cut planes. The actual calculated velocity values at the center plane ($\theta^+ = 1/2$) are larger than those at the corresponding location of the $\theta^+ = 5/6$ plane. Our numerical results show that the velocity profiles are symmetrical about $\theta^+ = 1/2$ plane, due to the symmetrical boundary conditions at the side walls. The velocity profiles along the θ direction have the parabolic behavior in the entrance region of the evaporator section. With increasing r/R, the velocity profiles along the θ direction become flattered due to the divergence of the vapor flow channel.

Figure 5 shows the dimensionless u velocity profiles along the center plane ($\theta^+ = 1/2$) in the evaporator zone for Re_h values of 10, 25, 50, 75, 100 and 150. As can be seen from Fig. 5, vapor accelerates in the evaporator section due to the vapor injection. The velocity maxima are shifted toward the bottom wall due to the injection from the top wall and suction at the bottom wall. With increasing Re_h values, the shifting is more prominent, giving an increase in the wall shear stress at the bottom wall and a decrease at the top wall. Like conventional symmetrical heat pipes, there is no flow reversal in the evaporator zone of the asymmetrical disk-shaped heat pipe.

Figure 6 shows the dimensionless u velocity profiles along the center plane ($\theta = 1/2$) over the condenser section. Vapor decelerates in the condenser section due to the vapor suction. The shifted velocity maxima gradually returns back to the center ($y/h = 1/2$) due to the symmetrical cooling condition over the condenser zone. For $Re_h = 50$, flow separation takes place which leads to a region of reversed flow at the top entrance region of the condenser zone. The flow separation always starts at the top entrance of the condenser zone ($r^+ = \varphi$) and results in a recirculating flow cell downstream. This also can be seen in Fig. 4. As Re_h

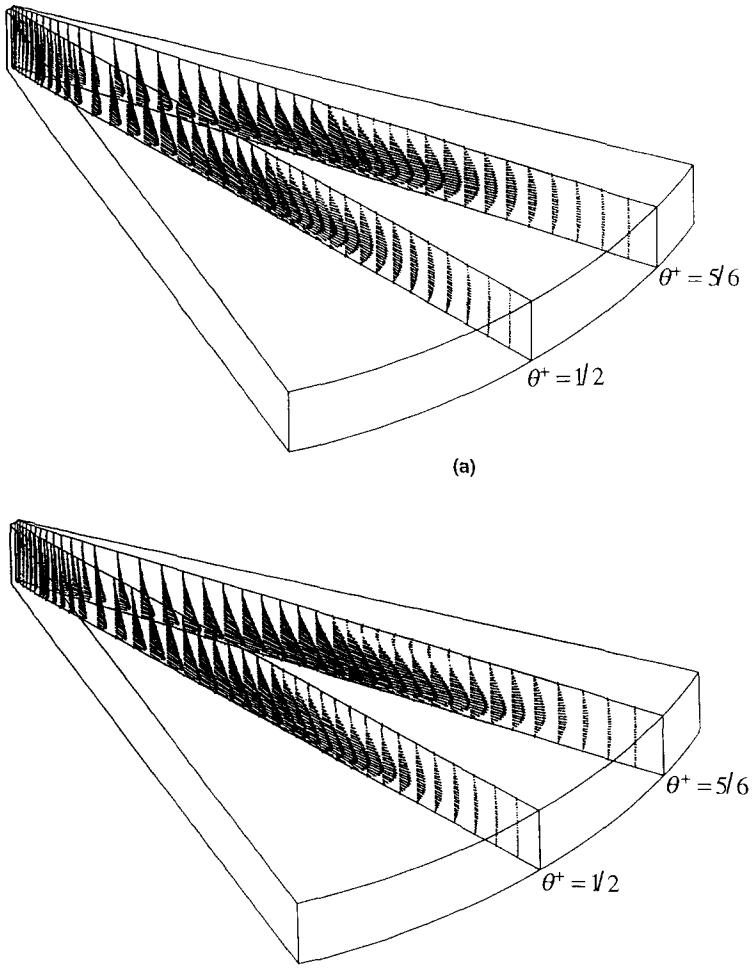

Fig. 4. Vapor flow field in the disk-shaped heat pipe for: (a) $Re_h = 50$; and (b) $Re_h = 100$.

value increases, the recirculation expands towards the end of the condenser section. This is different from the conventional symmetrical heat pipes [9] and the flat plate heat pipe investigated by Ooijen and Hoogendoorn [1], in which the wall separation point first occurs at the end of the condenser section and moves upstream as the injection Reynolds number increases. The reason for this difference is partly due to the steep change from vapor injection to suction at $r^+ = \varphi$ without an adiabatic section in between.

Figure 7 shows the vapor pressure distributions along the heat pipe. The pressure drop is plotted in dimensional form for θ^+ values of 1/6, 1/3 and 1/2. The transverse pressure differences in the y direction were found to be negligibly small. Therefore, a single graph was used to represent the pressure distribution along the heat pipe for all y values. As can be seen in Fig. 6, the pressure differences in the θ direction are negligible over both evaporator and condenser sections.

The vapor pressures in the evaporator section always decrease due to the frictional loss and the acceleration of the vapor flow caused by mass injection from the top wall. In the condensation zone, the pressure distributions represent the internal balance of the frictional loss and the pressure recovery owing to the deceleration of the vapor flow by mass suction. At low injection Reynolds number, such as $Re_h = 10$, the frictional effect dominates and the vapor pressure drops are observed over the condenser section. As the injection Reynolds number increases, the inertial effect becomes more dominant. For $Re_h = 25$, a constant pressure is found in the condenser section, indicating the same contributions of the frictional effect and the inertial effect. For higher Re_h values, the inertial effect becomes dominant and pressure build up occurs in the condenser section. The sharp pressure build up at the beginning of the condenser section is assumed to be attributed to the sudden change from mass injection to mass suction without an adiabatic zone in between. This effect along with the reduction in the pressure recovery due to the recirculation at the

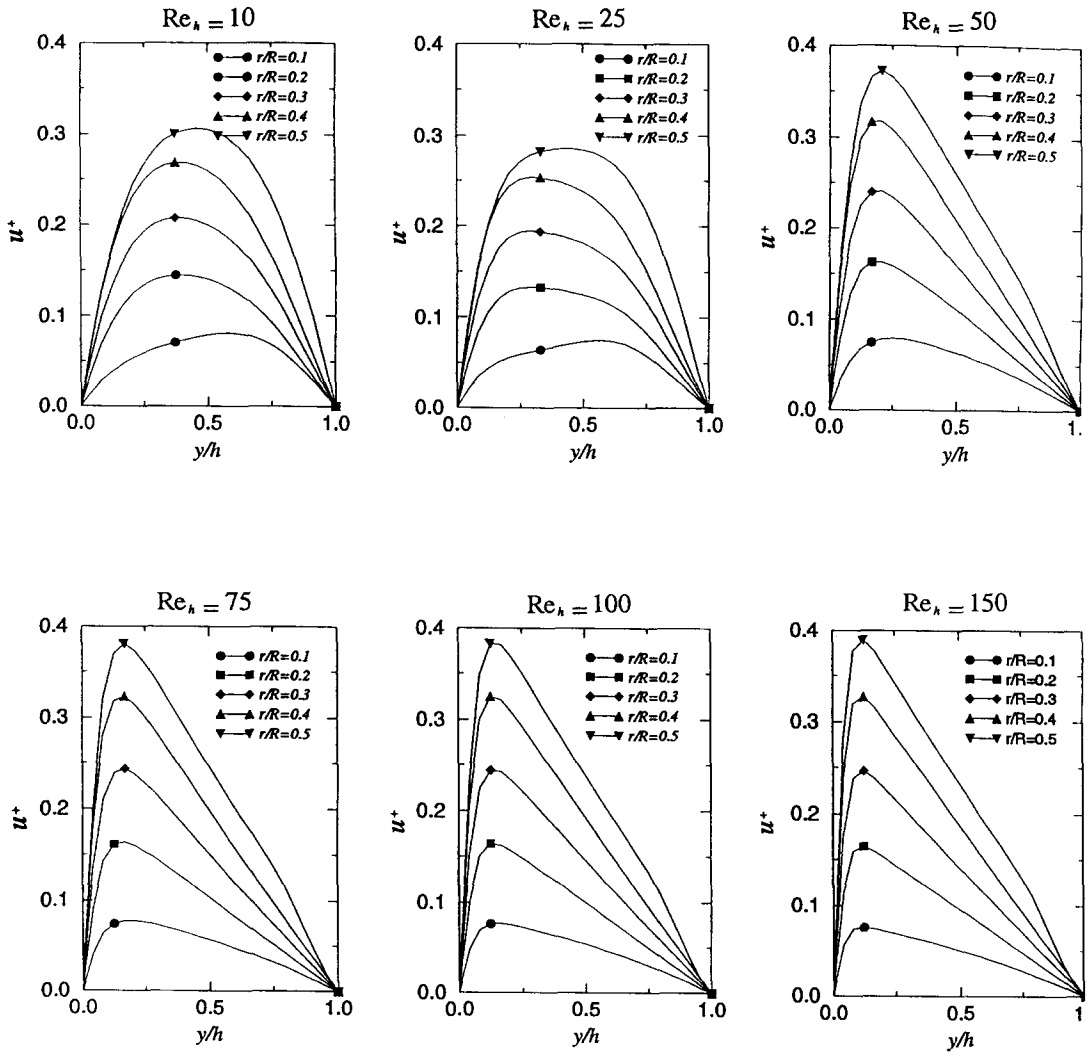

Fig. 5. Dimensionless u velocity profiles along the center plane ($\theta^+ = 1/2$) of the evaporator section.

top entrance of the condenser zone is responsible for the change of curvature in the pressure distribution at higher injection Reynolds numbers.

Analytical results

Figure 8 compares the analytical u velocity profiles along the heat pipe at the center plane ($\theta^+ = 1/2$) with the numerical prediction for Re_h values of 10, 25, 50, 75, 100 and 150. Both analytical and numerical models predict flow reversal at the top entrance of the condenser section for Re_h values of 50 and higher. The secondary flow starts at the beginning of the condenser section and expands downstream as the injection Reynolds number increases. No backflow was observed at the far end of the condenser zone even for higher values of Re_h. The agreement between the analytical results and the numerical simulation is very good over the entire vapor flow channel. This indicates that the analytical model can accurately describe vapor velocity profiles under conditions including strong flow reversal.

Figure 8 compares the analytical pressure distributions along the heat pipe with the numerical prediction for Re_h values of 10, 25, 50, 75, 100 and 150. The analytical results for all Re_h values shown agree very well with the numerical computations over the evaporation zone and fairly well in the condensation zone. Despite some discrepancy between the analytical predictions and the numerical calculations at the entrance region of the condenser section, the analytical and numerical overall pressure drops obtained agree very well.

CONCLUSIONS

A three-dimensional numerical analysis of vapor flow in an asymmetrical disk-shaped heat pipe has been carried out for the first time. The results show

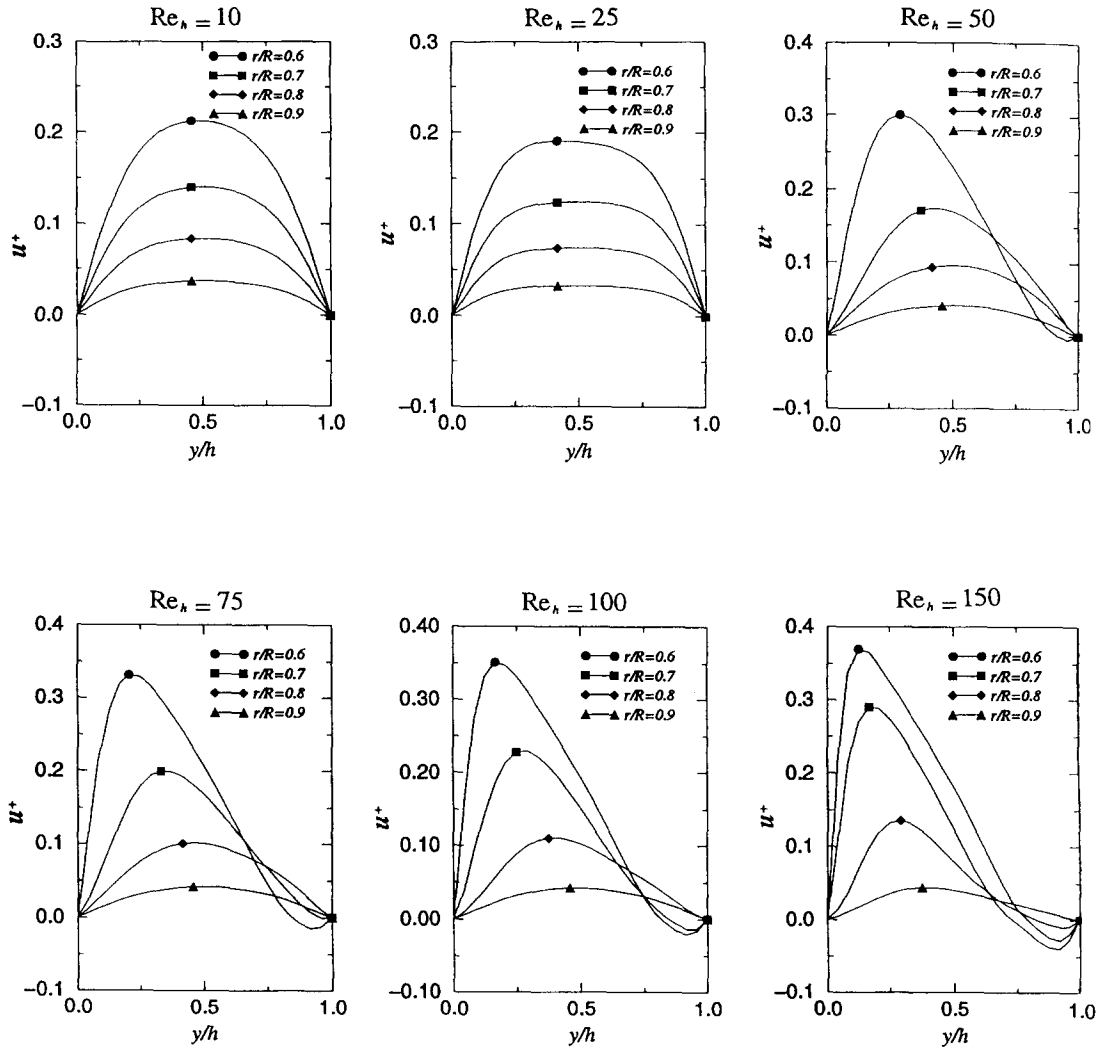

Fig. 6. Dimensionless u velocity profiles along the center plane ($\theta^+ = 1/2$) of the condenser section.

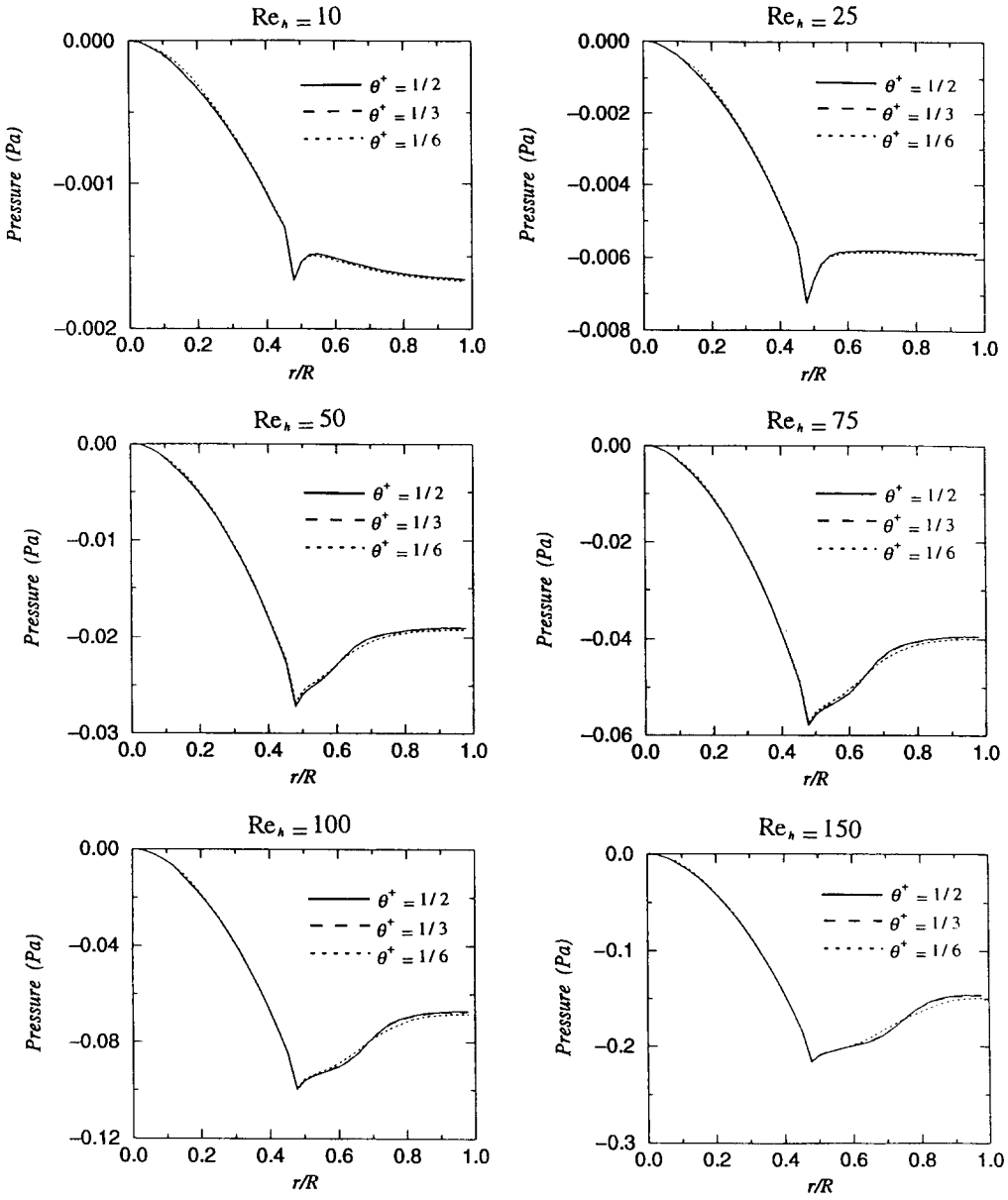

Fig. 7. Pressure distributions along the heat pipe.

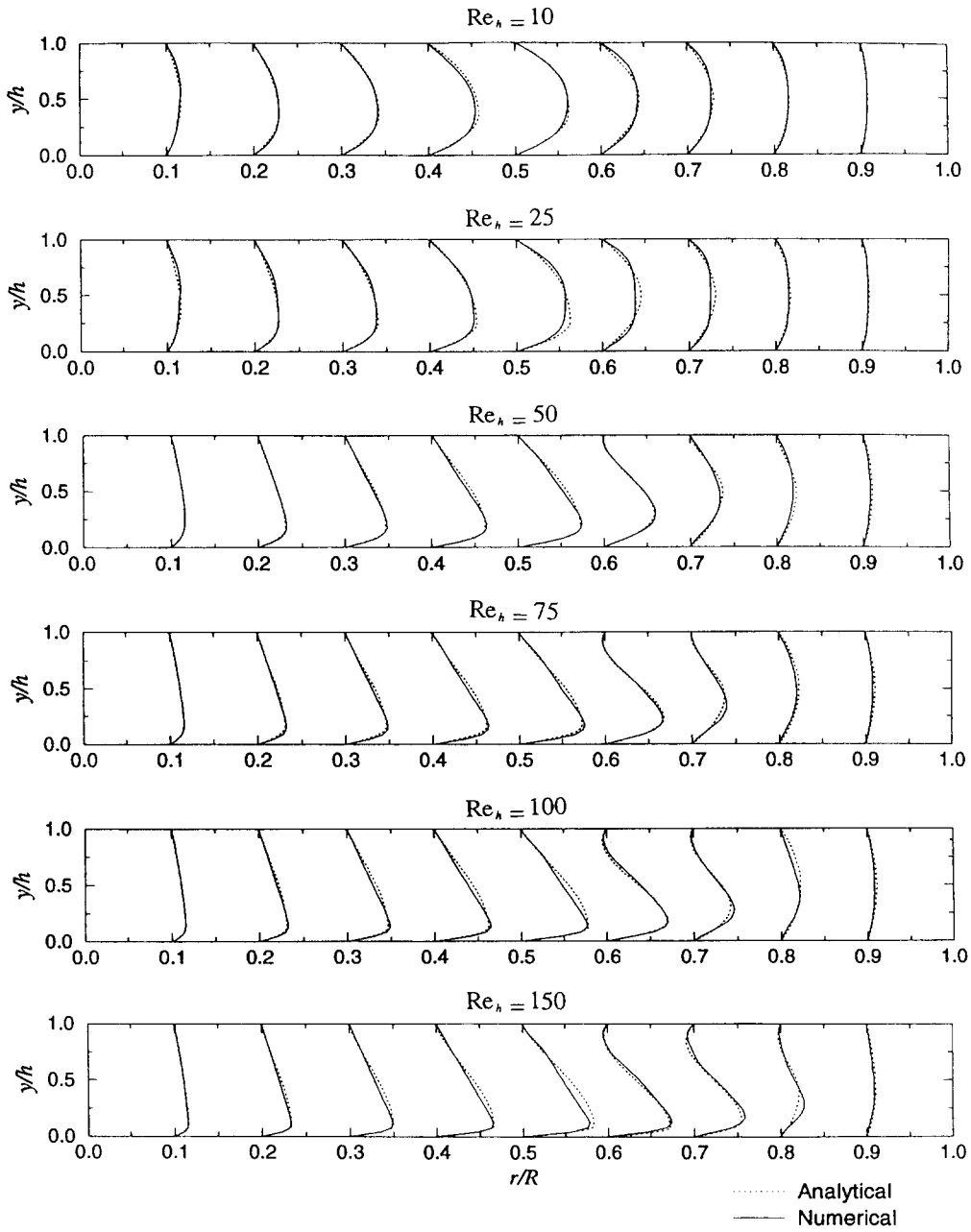

Fig. 8. Comparison of the numerical and analytical results of the velocity profiles along the center plane ($\theta^+ = 1/2$).

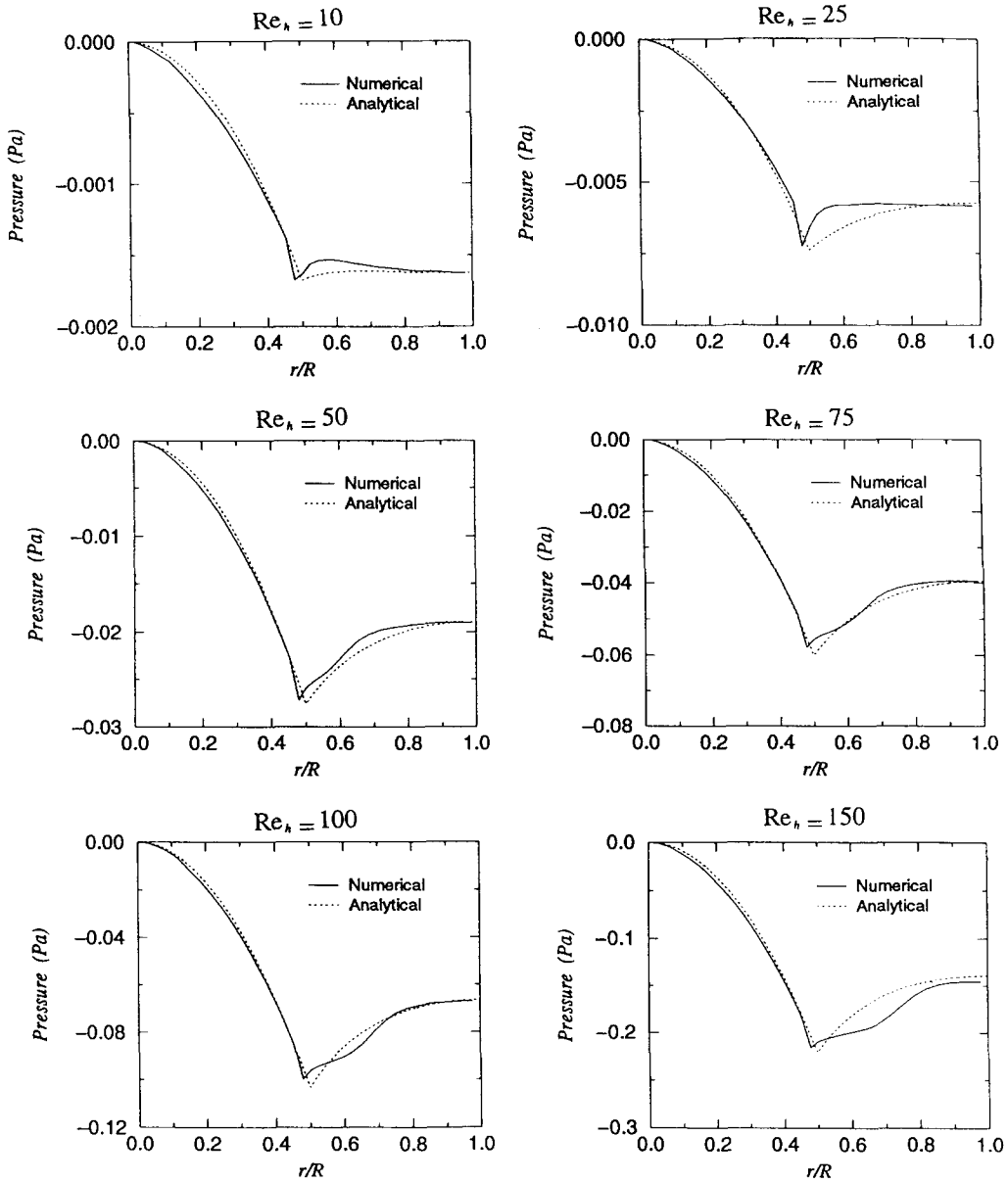

Fig. 9. Comparison of the numerical and analytical results of the pressure distributions.

in detail the characteristics of the three-dimensional model for the vapor flow in the disk-shaped heat pipe and the effects of the divergence of the vapor flow channel. A pseudo-three-dimensional analytical model has also been developed to predict the velocity profile and pressure drop along the heat pipe under conditions including strong flow reversal. In this work, it was established that the pressure variations in the transverse and angular directions are relatively small and that they can be neglected. The analytical solutions agree very well with the numerical results. While saving tremendous CPU time (more than five order of magnitude) and aiding in understanding the physical phenomena occurring in the problem, the analytical model provides a quick prediction method for the disk-shaped heat pipe operation and is very useful for practical engineering purposes.

Acknowledgements—This work was supported by the Department of Energy under grant number DE-FG02-93ER61612. The authors would like to thank Dr Thomas Blue for his help on this work.

REFERENCES

1. Ooijen, H. and Hoogendoorn, C. J., Vapor flow calculations in a flat-plate heat pipe. *AIAA Journal*, 1979, **17,** 1251–1259.
2. Vafai, K. and Wang, W., Analysis of flow and heat transfer characteristics of an asymmetrical flat plate heat pipe. *International Journal of Heat and Mass Transfer*, 1992, **35,** 2087–2099.
3. Vafai, K., Zhu, N. and Wang, W., Analysis of asymmetrical disk-shaped and flat plate heat pipes. *ASME Journal of Heat Transfer*, 1995, **117,** 209–218.
4. Zhu, N. and Vafai, K., Optimization analysis of a disk-shaped heat pipe. *AIAA Journal of Thermophysics*, 1996, **10,** 179–182.
5. Zhu, N. and Vafai, K., The effects of liquid–vapor coupling and non-Darcian transport on asymmetrical disk-shaped heat pipes. *International Journal of Heat and Mass Transfer*, 1996, **39,** 2095–2113.
6. Quaile, J. P. and Levy, E. K., Laminar flow in a porous tube with suction. *ASME Journal of Heat Transfer*, 1975, **97,** 66–71.
7. Bankston, C. A. and Smith, H. J., Vapor flow in cylindrical heat pipes. *ASME Journal of Heat Transfer*, 1973, **95,** 371–376.
8. Busse, C. A. and Loehrke, R. I., Subsonic pressure recovery in cylindrical condensers. *ASME Journal of Heat Transfer*, 1989, **111,** 533–537.
9. Taylor, C. and Hood, P., A numerical solution of the Navier–Stokes equations using the finite-element technique. *Computers and Fluids*, 1973, **1,** 73–89.
10. *FIDAP Theoretical Manual*. Fluid Dynamics International, Evaston, IL, 1993.
11. Busse, C. A. and Prenger, F. C., Numerical analysis of the vapour flow in cylindrical heat pipes. *Proceedings of the 5th International Heat Pipe Conference*, Part I, JATEC, Tokyo, Japan, 1984, pp. 214–219.